https://ntrs.nasa.gov/search.jsp?R=20180004010 2019-04-29T08:11:32+00:00Z

An evaluation of gravity waves and gravity wave sources in the Southern Hemisphere in a 7-km global climate simulation

L. A. Holt[a*], M. J. Alexander[a], L. Coy[b,c], C. Liu[e], A. Molod[b], W. Putman[b], and S. Pawson[b]

[a]*NorthWest Research Associates, 3380 Mitchell Lane, Boulder, CO 80301*

[b]*Global Modeling and Assimilation Office, NASA Goddard Space Flight Center, Greenbelt, Maryland*

[c]*Science Systems and Applications Inc, Lanham, Maryland*

[e]*Department of Physical and Environmental Sciences, Texas A&M University-Corpus Christi, Corpus Christi, Texas*

[*]Correspondence to: Laura A. Holt, NorthWest Research Associates, 3380 Mitchell Lane, Boulder, CO 80301.

Email: laura@nwra.com

In this study, gravity waves in the high-resolution GEOS-5 Nature Run are first evaluated with respect to satellite and other model results. Southern Hemisphere winter sources of nonorographic gravity waves in the model are then investigated by linking measures of tropospheric nonorographic gravity wave generation tied to precipitation and frontogenesis with absolute gravity wave momentum flux in the lower stratosphere. Finally, nonorographic gravity wave momentum flux is compared to orographic gravity wave momentum flux and compared to previous estimates. The results show that the global patterns in gravity wave amplitude, horizontal wavelength, and propagation direction are realistic compared to observations. However, like other global models the amplitudes are weaker and horizontal wavelengths longer than observed. The global patterns in absolute gravity wave momentum flux also agree well with previous model and observational estimates. The evaluation of model nonorographic gravity wave sources in the Southern Hemisphere winter shows that strong intermittent precipitation (greater than 10 mm per hr) is associated with gravity wave momentum flux over the South Pacific, whereas frontogenesis and less intermittent, lower precipitation rates (less than 10 mm per hr) are associated with gravity wave momentum flux near 60 degrees South. In the model, orographic gravity waves contribute almost exclusively to a peak in zonal mean momentum flux between 70 and 75 degrees South, while nonorographic waves dominate at 60 degrees South, and nonorographic gravity waves contribute a third to a peak in zonal mean momentum flux between 25 and 30 degrees South.

Key Words: gravity waves, gravity wave sources, nonorographic gravity waves, Southern Hemisphere, gravity wave momentum flux, high-resolution climate simulation

1. Introduction

Gravity waves are important drivers of circulation and transport in the middle atmosphere. They are currently included in most climate models via parameterizations due to computational limitations on resolution. The resolution required to resolve the full gravity wave spectrum is orders of magnitude higher than is employed by current climate models, which means that climate models will need to rely on gravy wave parameterizations for the foreseeable future. However, at this time gravity wave parameterizations remain poorly constrained by observations (Alexander *et al.* 2010). This contributes to large model biases in middle atmosphere temperatures and winds, especially in the Southern Hemisphere stratosphere (Butchart *et al.* 2011; McLandress *et al.* 2012).

Some studies show improvements in model biases when gravity wave parameterizations are tied to tropospheric sources of gravity wave generation (Beres *et al.* 2005; Charron and Manzini 2002; Song and Chun 2005; Richter *et al.* 2010). For example, Choi and Chun (2013) showed that wind biases in the Southern Hemisphere winter stratosphere were reduced in a global climate model when they included a convective gravity wave parameterization in addition to the existing gravity wave drag parameterization. Other studies have shown better model realism when the gravity wave parameterization is based on an intermittent source function (de la Cámara and Lott 2015). This is based on several papers that have shown the highly intermittent nature of gravity wave generation, both in observations and models (e.g., Hertzog *et al.* 2008, 2012; Jewtoukoff *et al.* 2015; Plougonven *et al.* 2013).

The main sources of gravity waves are orography, jets/fronts, and convection. It is generally thought that the distributions of these sources vary with latitude, with convection dominating in the Tropics and jets, fronts, and orography dominating in the midlatitudes (Plougonven and Zhang 2014). Orographic gravity wave momentum fluxes are typically several times larger than nonorographic gravity wave momentum flux and are concentrated over orographic features (e.g., Vincent *et al.* 2007; Hertzog *et al.* 2008; Jewtoukoff *et al.* 2015). Even though orographic gravity wave momentum fluxes are much larger than nonorographic gravity wave momentum fluxes locally, nonorographic gravity waves have been shown to contribute substantially to the total gravity wave momentum flux since they are generated over a much larger area (Hertzog *et al.* 2008). Convection is an important generation mechanism of nonorographic gravity waves in the troposphere (e.g., Alexander *et al.* 1995), and the importance of moisture has been highlighted in idealized models (Wei and Zhang 2014) and in case studies comparing simulations with a regional model to observations (Plougonven *et al.* 2015). Fronts are also known to be a major source of nonorographic gravity waves (Eckermann and Vincent 1993; Plougonven and Snyder 2007). However, the relative importance of different nonorographic gravity wave sources is still not completely understood.

This study examines gravity waves and their sources, with an emphasis on the Southern Hemisphere winter, in a 7-km horizontal resolution global climate model. Global models in general, and the model used in this study in particular, are good tools for this investigation because they have complete winds and temperatures output on a regular grid and high-resolution that resolves much of the gravity wave spectrum. We first validate the gravity wave properties and global distributions with respect to observations and other models. Then we examine the relationship between nonorographic gravity waves and sources. Finally we compare orographic and nonorographic gravity wave momentum flux.

The paper is organized as follows. In Section 2 we describe the model. In Section 3 we validate the model's gravity waves by first comparing them to those observed by the Atmospheric Infrared Sounder (AIRS) and then computing the January and July absolute gravity wave momentum flux and comparing it to previous model estimates. In Section 4 we relate the absolute gravity wave momentum flux in the lower stratosphere to proxies of tropospheric wave generation. In Section 5 we compare the momentum fluxes generated by orographic gravity waves to those generated by nonorographic gravity waves. Finally, we provide a summary and closing remarks in Section 6.

2. GEOS-5 Nature Run

The Nature Run (NR) is a global non-hydrostatic, 7-km horizontal resolution mesoscale simulation produced by the Goddard Earth Observing System (GEOS-5) atmospheric general circulation

model (Gelaro *et al.* 2015; Putman *et al.* 2014) with finite-volume (FV) dynamics (based on Lin (2004)) on a cubed-sphere horizontal grid (Putman and Lin 2007). The main purpose of the NR is conducting observation system simulation experiments (OSSEs) to test proposed observing system designs, but here we take advantage of the existing high-resolution simulation to study gravity waves. The NR simulation was run for roughly 2 years, from May 2005 to June 2007, with 72 vertical levels from the surface up to ∼0.01 hPa (∼85 km). The vertical resolution is ∼200 m or less below 800 hPa, ∼500 m near 600 hPa, ∼1 km near the tropopause, and ∼2 km near the stratopause. The physics, remapping, and dynamics time steps were 300, 75, and 5 s, respectively. The NR was forced with prescribed sea-surface temperature and sea-ice at 0.25° resolution, biomass burning emissions (organic and black carbon aerosols, SO_2, CO, and CO_2) at 0.1° resolution, and anthropogenic emissions (aerosols, CO, CO_2, SO_2, SO_4) at 0.1° resolution (for details see Putman *et al.* 2014).

The NR is in the "gray zone" of atmospheric model resolution, where the resolution is high enough to start resolving smaller-scale processes like convection but not high enough to resolve them completely. Models in the gray zone still need to rely on parameterizations to some degree, but these parameterizations can be relaxed compared to coarser resolution models. Convection in GEOS-5 is parameterized using the Relaxed Arakawa-Schubert (RAS) scheme of Moorthi and Suarez (1992). As resolution increases, the RAS is controlled by a stochastic limit on deep convection (Tokioka *et al.* 1988), which basically confines the RAS to function as a shallow convection scheme. Another resolution-aware parameterization in GEOS-5 is the orographic gravity wave parameterization (McFarlane 1987). Parameterized orographic waves are forced by sub-grid scale variance, which is scaled down with increasing resolution to account for the increase in resolved waves produced by the dynamics of the model.

Even with a very high horizontal resolution, the NR still required a non-orographic gravity wave parameterization (based on Garcia and Boville 1994) to achieve realistic gravity wave drag and circulation in the middle atmosphere. Holt *et al.* (2016) discussed this issue in depth for the tropics and concluded that non-orographic gravity wave generation was realistic in the NR but that the non-orographic gravity wave parameterization was necessary because the resolved waves were too heavily dissipated by the model. The NR included explicit diffusion from second-order divergence damping, which provided a strong damping on the resolved gravity waves. Parameterized non-orographic gravity waves were specified with an equatorial peak in momentum flux (see Figure 3 in Molod *et al.* (2015)), and the phase speed spectrum was launched from 400 hPa with a range of ± 40 m s^{-1} in increments of 10 m s^{-1}.

For the analysis of the NR in this paper, we used 30-minute instantaneous output that was interpolated from the cubed-sphere grid to a 0.0625° × 0.0625° (lon × lat) grid while maintaining the full model vertical grid. We also used hourly instantaneous output interpolated to 0.5° × 0.5° (lon × lat) horizontal resolution also maintaining the full model vertical grid.

3. Validation of the gravity waves in the NR

3.1. Comparison to AIRS

The AIRS instrument on NASA's Aqua satellite provides global coverage of infrared radiance spectra in three spectral bands between 3.74 and 15.4 μm. The 4.3 and 15 μm CO_2 bands have been used extensively to study gravity waves in the stratosphere (e.g., Alexander and Teitelbaum 2007; Gong *et al.* 2012; Hoffmann *et al.* 2013, 2014, 2016). Here we use the AIRS 4.3 μm channel average brightness temperatures described in Hoffmann and Alexander (2010). AIRS uses cross-track scanning, where each scan consists of 90 footprints over 1780 km (at the ground) and is separated by 18 km along-track distance. The footprint size varies with the scanning angle between 14×14 km^2 and 21×42 km^2 (see Figure 2 in Hoffmann *et al.* (2014)).

To obtain AIRS brightness temperature anomalies, background variations first need to be removed. Additionally, AIRS raw radiances have a limb-brightening in the cross-track direction that needs to be removed before studying the small-scale waves. As is traditionally done with AIRS, a fourth-order polynomial fit in the x-direction was used to remove the background at each y-location, where the x-direction refers to cross-track scanning and the y-direction refers to along-track scanning. In addition to removing the limb-brightening effect, this method removes larger-scale wave perturbations with horizontal wavelengths longer

than ∼500 km. Figure 1 shows an example of the AIRS brightness temperature anomalies on 26 July 2005 in the Southern Hemisphere.

Figure 1 also shows NR brightness temperature anomalies sampled at the AIRS measurement locations for the same day. For the NR, brightness temperatures were estimated as the vertical average temperature weighted by the AIRS kernel function, which has a broad peak between 30–40 km altitude (see Figure 3 in Hoffmann and Alexander 2010). Brightness temperature anomalies were then obtained by subtracting the large-scale background (>500 km). The background was approximated using a spherical harmonic series truncated at horizontal wavenumber n=80 with an exponential taper (Sardeshmukh and Hoskins 1984). Finaly, the NR brightness temperature anomalies were sampled at AIRS footprints. The dates for the NR and AIRS are the same, but since the NR is a climate model the individual wave features are not expected to be exactly the same. However, qualitatively both fields have a similar overall pattern around Antarctica, with especially notable agreement over South America and the Antarctic Peninsula. The amplitudes of the NR anomalies are about a factor of 4 smaller than the amplitudes of the AIRS anomalies. This is attributed to excessive model dissipation and will be discussed in more detail below. Another difference between AIRS and the NR is in the latitude of the waves South of Australia that are farther north in the observations. Also note that the NR plot is smoother than the AIRS plot, most likely because of the noise inherent in observations. This date is typical of the similarity found between the AIRS observations and the NR simulation.

To evaluate and compare NR and AIRS gravity wave occurrence frequencies, amplitudes, horizontal wavelengths, and horizontal propagation directions, we analyzed waves with the basic method described in Alexander and Barnet (2007). We applied this analysis to both the AIRS and the AIRS-sampled-NR brightness temperature anomalies for July 2005. The brightness temperature anomalies were interpolated to give constant 13.4 km spacing in x. Then the S-transform was applied to the brightness temperature anomalies to give the complex transform $\tau(\lambda_x, x)$, and the covariance spectrum between the two rows adjacent in y was computed. This covariance spectrum was integrated in x, excluding signals within the "cone of influence" that are affected by the edges of the observation swath (e.g., Woods and Smith 2010).

To identify dominant waves for further analysis, the covariance spectra were averaged ±5 rows ahead and behind in the y-direction, and up to 8 peaks in the covariance λ_x spectrum were identified. This averaging was done to ensure that the identified signals ($\lambda_{x_i}, i \leq 8$) were coherent waves occurring across multiple rows of data, and thus helping to eliminate the effects of noise. Now returning to the individual two-row-covariance spectrum, we focused only on these identified signals and computed the phase shift $\Delta\phi_i$ in the y-direction, where $\Delta\phi_i$ is the angle whose tangent is the ratio of imaginary to real components of the complex covariance. The y-wavelength is given by $\lambda_{y_i} = \Delta y/\Delta\phi_i$, where Δy is the spacing between rows. The net wave amplitude at each point along the swath was then computed by summing the identified signal amplitudes $\hat{T} = \Sigma_i \hat{T}_i$. Wavelengths at each point were computed as weighted sums, $\lambda_x = (\Sigma_i \lambda_{x_i} \hat{T}_i)/\hat{T}$ and $\lambda_y = (\Sigma_i \lambda_{y_i} \hat{T}_i)/\hat{T}$. The values of λ_y were also smoothed with a triangular 3-point smoothing in the y-direction. The horizontal wavenumber, k, and orientation of phase lines, θ, relative to the x-direction were computed via

$$k = \left(\frac{1}{\lambda_x^2} + \frac{1}{\lambda_y^2}\right)^{\frac{1}{2}} \tag{1}$$

and

$$\theta = \tan^{-1}\left(\frac{\lambda_y}{\lambda_x}\right) \tag{2}$$

Finally, with the known angle of the measurement swath relative to the cardinal directions, the wave orientation direction was computed relative to east with 180-degree ambiguity. Positive angles represent waves propagating northeast/southwest, while negative angles represent waves propagating southeast/northwest. We can break the ambiguity with the assumption that waves observed by AIRS must have long vertical wavelengths, and are thus propagating upstream against the local wind. Since stratospheric winds are eastward in winter and westward in summer, waves seen in AIRS data generally propagate westward in winter and eastward in summer (Ern *et al.* 2017).

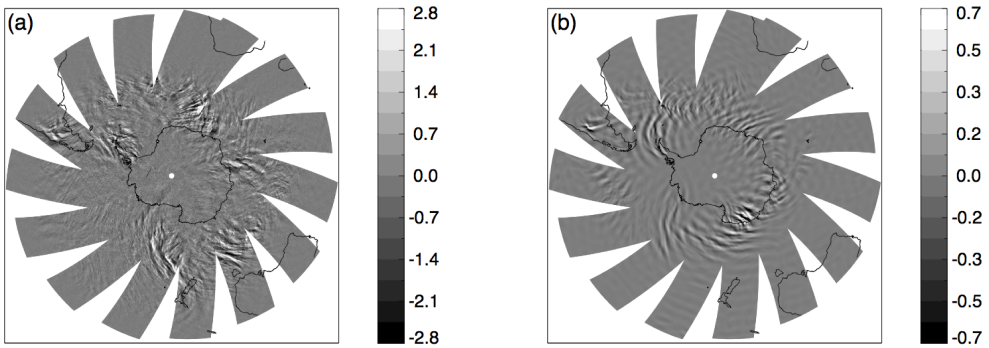

Figure 1. Southern hemisphere brightness temperature anomalies on 26 July 2005 for (a) AIRS and (b) the NR near ∼35 km. Note the different color bar ranges. The NR is a climate model, so individual wave features differ because of different meteorological conditions.

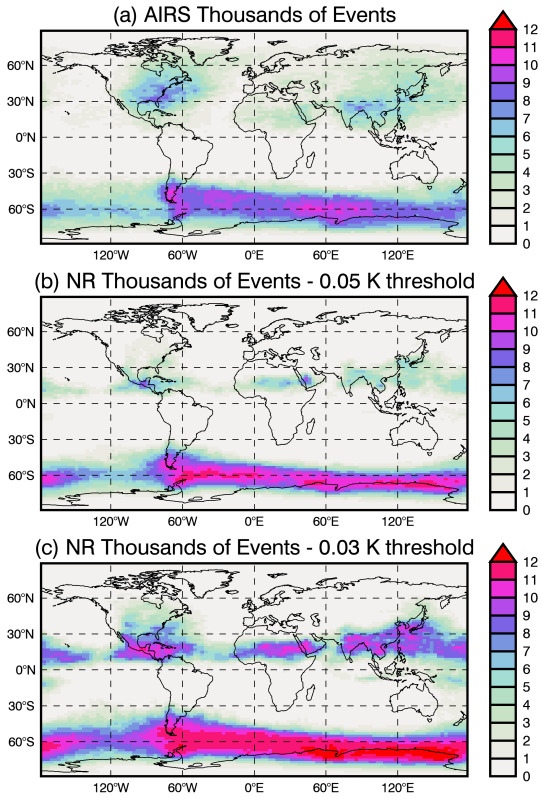

Figure 2. July average number of detected wave events near ∼35 km for (a) AIRS and the NR with (b) 0.05 K and (c) 0.03 K detection thresholds.

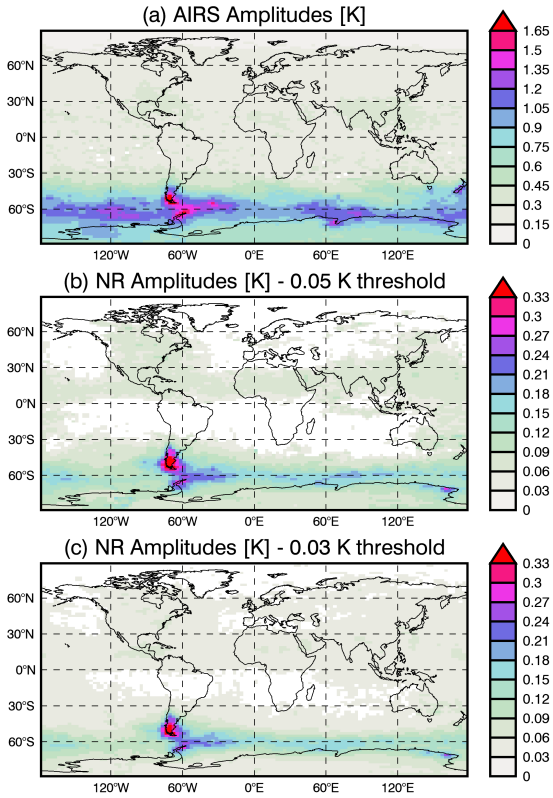

Figure 3. July average wave amplitude near ∼35 km for (a) AIRS and the NR with (b) 0.05 K and (c) 0.03 K detection thresholds. White boxes indicate where not enough data was above the given threshold. Note the different ranges on the color bars. The NR color bars values are 5× smaller than the AIRS color bar values.

To create a map of average wave properties, the local amplitude-weighted means were computed. All of the AIRS results were filtered to only include signals with covariance greater than $3\sigma_N$, where σ_N is the standard deviation of the noise covariance amplitude and is a function of temperature (see Figure 6 in Hoffmann *et al.* 2014). We chose $3\sigma_N$ because it excludes unwanted noise and retains a good signal. For the NR the results were filtered with a constant threshold value since the model obviously does not have the instrument noise.

Figure 2 shows the July average number of detected wave events for AIRS and the NR. Since the AIRS weighting function peaks between 30 and 40 km, Figures 1–5 can be taken to be near ∼35 km. For the NR, two threshold values (0.03 K and 0.05 K) are plotted to illustrate the sensitivity of the results to the choice of threshold value. Since the number of events is dependent on the somewhat arbitrary choice of threshold value, the most important information that this plot reveals is that the July average

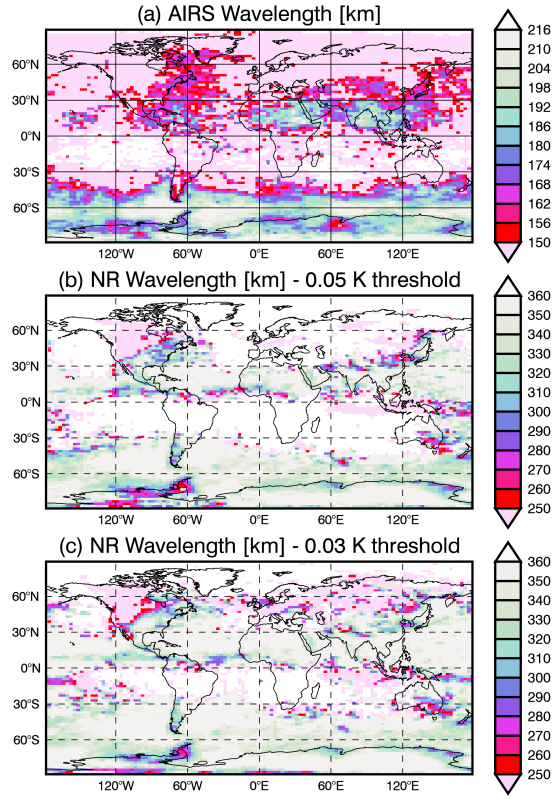

Figure 4. July average wavelength near ∼35 km for (a) AIRS and the NR with (b) 0.05 K and (c) 0.03 K detection thresholds. White boxes indicate where not enough data was above the given threshold. Note the different ranges on the color bars. The NR color bar values are $\frac{5}{3}\times$ the AIRS color bar values.

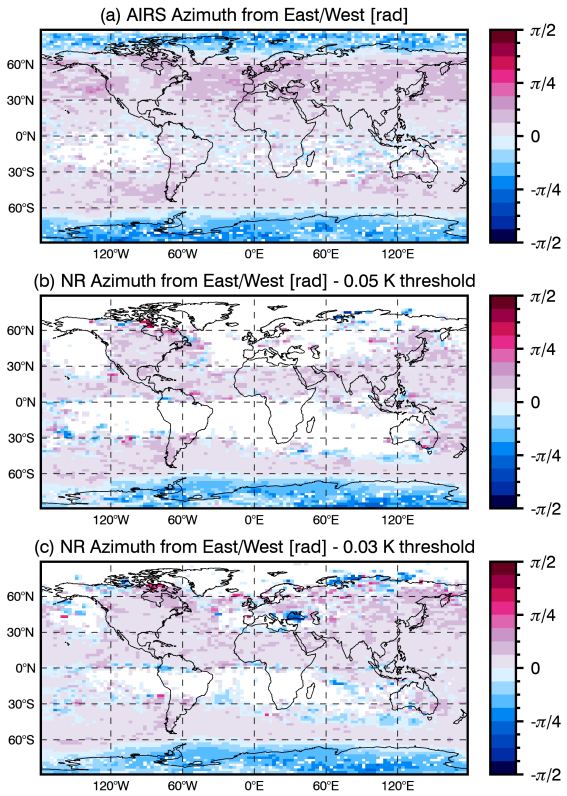

Figure 5. July average azimuth near ∼35 km for (a) AIRS and the NR with (b) 0.05 K and (c) 0.03 K detection thresholds. White boxes indicate where not enough data was above the given threshold. Positive angles represent waves propagating northeast/southwest, while negative angles represent waves propagating southeast/northwest.

number of wave events detected in the NR and AIRS have similar global patterns in the winter hemisphere. In the summer hemisphere, the differences are most likely due to time differences between the NR and AIRS sampling. As noted above, the NR brightness temperatures were interpolated spatially to the AIRS measurement locations. However, we chose not to interpolate in time to the AIRS measurements so as not to wash out the waves in the NR brightness temperatures. Since the timing of convection is so important for generating waves, the time differences between the NR and AIRS sampling most likely explain the differences in the summer hemisphere. The convective parameterization could also be important (Kim *et al.* 2007).

Figure 3 shows the July average amplitudes near ∼35 km for AIRS and the NR. In general the global patterns agree well, with a band of larger amplitude waves around 60°S and the largest amplitude waves over the southern tip of South America and the Antarctic peninsula. However, the AIRS amplitudes are more evenly distributed over all longitudes whereas the NR amplitudes are more concentrated over the southern tip of South America and the Antarctic peninsula. Another significant difference between AIRS and the NR is that the average amplitudes in the NR are between ∼4 and 5 times smaller than the average amplitudes in the AIRS data. The average amplitude is not very sensitive to the NR threshold value in the Southern Hemisphere winter where the wave amplitudes are typically large.

The underestimation of observed GW amplitudes, and therefore momentum flux, is common in global climate simulations and has been shown previously for the high horizontal resolution NR (Holt *et al.* 2016) and other models. Holt *et al.* (2016) showed that NR resolved gravity wave drag in the tropics in the quasi-biennial oscillation (QBO) region was too low compared to the zonal force required to drive the observed QBO (inferred from the MERRA-2 reanalysis). They attributed this to a combination of low vertical resolution and dissipation in the NR. Jewtoukoff *et al.* (2015) found a large discrepancy between the magnitude of momentum fluxes at 70 hPa derived from Concordiasi balloon observations and in the European Centre for Medium-Range Weather Forecasts (ECMWF) model. The momentum fluxes in ECMWF were on average a factor of 5 smaller than the momentum fluxes derived from the balloon observations. They discussed the spectral truncation of ECMWF and numerical

diffusion as possible reasons for the underestimate. The ECMWF analyses used by Jewtoukoff *et al.* (2015) had a horizontal resolution of about 16 km and vertical resolution of about 500 m, whereas the NR horizontal resolution is about 7 km and vertical resolution is between about 1 and 2 km in the stratosphere. Note also the different altitudes for the NR and ECMWF in this paragraph. The NR amplitudes are about a factor of 4–5 (a factor of 16–25 in momentum flux) lower than the AIRS amplitudes near 35 km, and ECMWF momentum fluxes are about a factor of 5 lower than the Concordiasi momentum fluxes near ∼19–20 km. In the next section, we will show that at ∼20 km, the NR is actually very similar to ECMWF in terms of the mean gravity wave momentum flux.

Figure 4 shows the July average wavelengths for AIRS and the NR. AIRS wavelengths are on average ∼2 times smaller than NR wavelengths. The global patterns are again similar between AIRS and the NR, with smaller wavelengths over the southern tip of South America and the mountainous regions of Antarctica. As with amplitude, the average wavelength is also not very sensitive to the NR threshold, especially in the Southern Hemisphere. The larger average horizontal wavelengths in the NR compared to AIRS reinforces the conclusions of (Holt *et al.* 2016) that the smaller-scale gravity waves in the NR are underrepresented due to either excess dissipation or low vertical resolution. Again, this problem is not unique to the NR and has been demonstrated in previous studies. For example, Preusse *et al.* (2014) showed that gravity wave horizontal wavelengths in ECMWF were at least 3 times longer than those estimated from the High Resolution Dynamics Limb Sounder (HIRDLS) observations for convective gravity waves between 40°S and 40°N.

Figure 5 shows the July average propagation direction (azimuth) for AIRS and the NR. As mentioned above, the wave propagation direction has a 180-degree ambiguity. The waves in Figure 5 are propagating southwest/northeast for positive angles ($0 < \theta \leq \frac{\pi}{2}$) and northwest/southeast for negative angles ($-\frac{\pi}{2} \leq \theta < 0$). In the Southern Hemisphere, the background winds are eastward in winter so we assume that the waves are propagating westward against the background wind. This means that waves with positive angles (red) are propagating southwest and waves with negative angles (blue) are propagating northwest. Previous studies have shown that waves have a tendency to propagate into the winter jet (e.g., Sato *et al.* 2009), and both AIRS and the NR show waves propagating into the winter jet. Furthermore, NR propagation directions agree very well with AIRS.

3.2. *Evaluation of NR Absolute Gravity Wave Momentum Flux*

To further validate the NR gravity waves, we calculated absolute gravity wave momentum fluxes for comparison to Geller *et al.* (2013), which was the first international collaborative effort at direct comparisons of global gravity wave momentum fluxes in observations and models. Because satellite methods only permitted estimates of the absolute values of momentum flux with no knowledge of direction, similar estimates of absolute momentum flux were computed and compared. Some of the models were high resolution, permitting an analysis of the resolved gravity waves. Others were coarse resolution, so the gravity wave fluxes were obtained from the model parameterizations of gravity wave drag.

We estimated the absolute gravity wave momentum flux for resolved waves in the NR using wind and temperature quadratics (u'^2, v'^2, w'^2, T'^2) as in Equation (1) in Geller *et al.* (2013):

$$\mathbf{M}^2 = \left(1 - \frac{f^2}{\hat{\omega}^2}\right) \rho_0^2 \left[\left(\overline{u'w'}\right)^2 + \left(\overline{v'w'}\right)^2\right]$$

$$= \rho_0^2 \overline{w'^2} \left(\overline{u'^2} + \overline{v'^2}\right) \left[1 - \frac{f^2}{\hat{\omega}^2}\right] \left[1 + \frac{f^2}{\hat{\omega}^2}\right] \qquad (3)$$

where

$$\frac{f^2}{\hat{\omega}^2} = \frac{f^2 g^2 \overline{T'^2}}{\overline{w'^2} N^4 T_0^2}. \qquad (4)$$

T_0 and ρ_0 are large-scale temperature and density, respectively. N is the Brunt–Väisälä frequency, f is the Coriolis parameter, $\hat{\omega}$ is the gravity wave intrinsic frequency, and g is Earth's gravity. Primes denote variations smaller than this large scale, which is taken to be 1000 km. The large-scale was approximated by a spherical harmonic series truncated at horizontal wavenumber n=40 with an exponential taper. The overbars denote averages

over 10° longitude × 5° latitude geographical bins. The terms in brackets on the right-hand side of Equation 3 represent a low-frequency correction. However, the correction only changed the global mean absolute gravity wave momentum flux by less than 3%.

Figure 6 shows the absolute gravity wave momentum flux at ∼20 km for January 2006 of the NR and also for January 2006 of the CAM5 run presented in Geller *et al.* (2013) for comparison. Two CAM5 experiments were initialized on 1 June 2005 and run at ∼0.25° horizontal resolution with observed sea-surface temperatures for 18 months. Figure 6 shows the average of the two CAM5 runs. The absolute gravity wave momentum fluxes for CAM5 were also calculated with Equation (3). The NR and CAM5 have very similar global patterns of absolute gravity wave momentum flux. In particular, both models have maxima over topographic features in the winter hemisphere. In the NR the largest maximum is over the Rocky Mountains, whereas the largest maximum in CAM5 is over the Tibetan Plateau. The global mean values are also shown at the top of the panel for both models. The NR global mean value is double the CAM5 global mean value. For comparison, the NR has roughly four times the number of horizontal grid points that the CAM5 simulation has. The global mean momentum fluxes in the NR are between 2.4 and 3 times weaker than parameterized gravity waves in the coarse resolution models in the Geller *et al.* (2013) comparison.

Figure 7 shows the absolute gravity wave momentum flux at ∼20 km for July 2006 of the NR and also for July 2006 of the CAM5 run presented in Geller *et al.* (2013) for comparison. As for January, the NR and CAM5 have very similar global patterns of absolute gravity wave momentum flux. In the winter hemisphere, both the NR and CAM5 have orographic maxima over the Antarctic Peninsula and the southern tip of South America. Both also show a large area of nonorographic flux over the Southern Ocean and into the Indian, South Atlantic, and South Pacific Oceans. In the summer hemisphere, the patterns of secondary maxima agree remarkably well.

The Geller *et al.* (2013) results showed large disparities among different observational estimates of the flux, and large differences between observations and models, which spoke to the remaining large uncertainty in the observational estimates. However, one surprising result was how three different climate models with six (two each, orographic and non-orographic) different gravity wave parameterization methods all showed rather similar gravity wave momentum fluxes. Since the different parameterization methods had all been tuned to give realistic simulations of the general circulation, perhaps in hindsight this result should not have been surprising. On the other hand, the resolved waves in two high-resolution models, while showing very similar global patterns both to each other and to the observations, had very different flux magnitudes. The CAM5, shown in our Figures 6 and 7, had the weakest fluxes among the models, and this is likely due to the very poor vertical resolution and higher dissipation. The other high-resolution model was Kanto (Watanabe *et al.* 2008), a spectral model with very high vertical resolution and minimal dissipation, and it showed the largest momentum fluxes among all of the models.

Table 1 lists the fluxes from the different models and observations in Geller *et al.* (2013) and the NR fluxes for January and July. The NR is between Kanto and CAM5 in terms of magnitude. While the NR has almost an order of magnitude higher horizontal grid-spacing than Kanto, Kanto has a much higher vertical grid-spacing and also very low dissipation at the smallest model scales (Watanabe *et al.* 2008). This most likely explains why the Kanto gravity wave momentum flux is almost 5 times larger than the NR. The observational estimates are between 1.4 and 3.1 times larger than the NR. However, as noted above the uncertainty in the satellite estimates is large, and previous studies have shown that satellite estimates tend to have a low bias (e.g., Ern *et al.* 2004). Therefore, the NR is most likely several factors too low compared to reality.

As mentioned above, Jewtoukoff *et al.* (2015, Fig 1) compared gravity momentum fluxes from Concordiasi to those from ECMWF at ∼19–20 km for the Southern Hemisphere (poleward of ∼45°S), averaged over September 2010–January 2011. The mean momentum flux was 9 mPa for Concordiasi and 1.8 mPa for ECMWF. The NR mean momentum flux poleward of ∼45°S in July is 1.7 mPa, which is comparable to ECMWF. It is worth noting that for the NR we removed scales larger than ∼1000 km to obtain estimates of gravity wave momentum flux, while Jewtoukoff *et al.* (2015) removed scales larger than ∼2667 km.

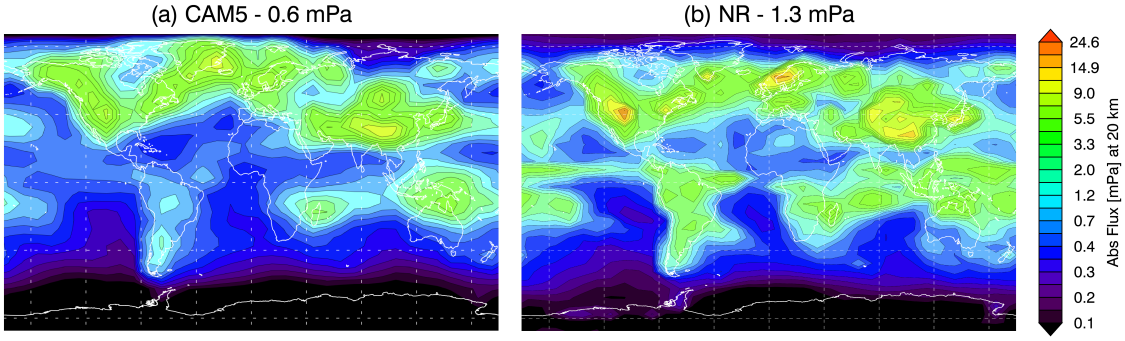

Figure 6. Monthly mean absolute gravity wave momentum fluxes for (a) January 2006 of the CAM5 run presented in Geller *et al.* (2013) and (b) January 2006 of the NR at 20 km. The global mean values for each model are shown above each panel.

Table 1. Global mean absolute gravity wave momentum fluxes at 20 km (in mPa) for the NR and results from the different models (Kanto, CAM, GISS, ECHAM, HadGEM) and observations (HIRDLS1, HIRDLS2) in Geller *et al.* (2013).

	NR	Kanto	CAM	GISS	ECHAM	HadGEM	HIRDLS1	HIRDLS2
Jan	1.3	6.29	0.6	3.15	3.54	3.99	1.82	2.17
Jul	1.3	6.29	0.5	3.29	3.39	4.02	4.06	2.19

So while the comparison here is not apples to apples since there are differences in time of year, slight differences in altitude, and differences in the background removal, it shows that the NR is similar to other global models.

The results of the comparison to AIRS in the previous section and the comparison to other models in this section show that the global patterns in gravity wave properties are very realistic compared to observations, although like other global models the amplitudes are weaker and horizontal wavelengths longer than observed. However, the realism of the geographic variations in wave properties gives confidence that the wave sources and propagation are realistic in the NR.

3.3. Comparison of NR precipitation to GPM

Precipitating systems are a major source of gravity waves at mid to high latitudes (e.g., Choi and Chun 2013). To evaluate NR precipitation in the Southern Hemisphere winter, Figure 8 compares NR precipitation to precipitation retrievals from the Global Precipitation Measurement (GPM, Hou *et al.* 2014) Core Observatory. GPM Core Observatory extends the coverage of precipitation measurements to higher latitudes ($\sim 65°$S$-65°$N). We have used precipitation rates derived from the 13.6 GHz Ku-band precipitation radar reflectivity at pixel level with $\sim$5 km resolution (Seto *et al.* 2013) for this comparison. Figure 8 shows the precipitation PDFs for both orographic and nonorographic regions between 66° and 15°S for precipitation rates between 10 and 100 mm hr^{-1}. Here we have used precipitation rate squared on the x-axis since precipitation is proportional to latent heating, and latent heating squared is proportional to momentum flux (e.g., Beres *et al.* 2004). Orographic and nonorographic regions are defined in Figure 9 as described below. In general, the NR decently reproduces occurrences of precipitation rates below 20 mm hr^{-1} (Figure 8a). However, it significantly underestimates precipitation rates above 30 mm hr^{-1} over orographic regions (Figure 8b). Over nonorographic regions, the NR shows good agreement with GPM over both the low and high precipitation rates. This is especially relevant as we explore nonorographic gravity wave sources in the next section.

Figure 9 shows the geographical bins flagged as orographic (gray) based on the Global Land One-kilometer Base Elevation (GLOBE) dataset (Hastings and Dunbar 1999). We followed the method for flagging orographic bins used by Vincent *et al.* (2007): we first computed the gradient of the GLOBE elevation dataset at the 1 km resolution. Then the mean of the 10% largest gradients were calculated for each 10° longitude $\times$ 5° latitude bin. Finally, bins were flagged as orographic when this value exceeded 15 m km^{-1}. Additionally, some bins that are located in the lee of major orography (e.g., east of the Antarctic peninsula) were also flagged as orographic. This categorization of geographical bins into orographic and nonorographic is of

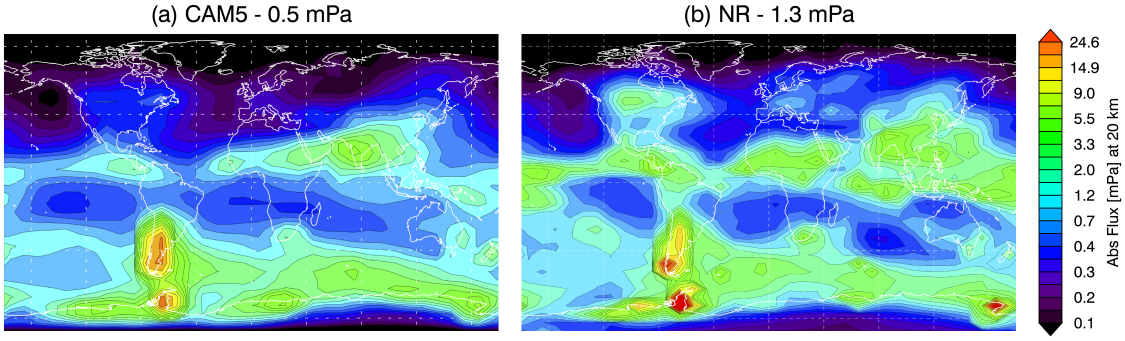

Figure 7. Monthly mean absolute gravity wave momentum fluxes for (a) July 2006 of the CAM5 run presented in Geller *et al.* (2013) and (b) July 2006 of the NR at 20 km. The global mean values for each model are shown above each panel.

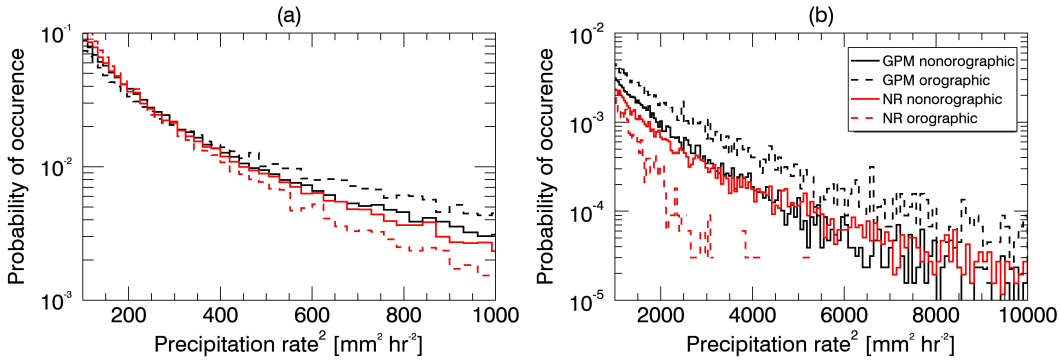

Figure 8. July precipitation PDFs for the NR and GPM for both orographic and nonorographic regions between $\sim 65^\circ$S-15°S for precipitation rates between (a) 10 and $\sim$31.6 and (b) $\sim$31.6 and 100 mm hr^{-1}. GPM Ku near surface precipitation rates for July 2014 and 2015 were used to calculate the GPM PDFs. NR July 2015 surface precipitation rates were used to calculate the NR PDFs. Orographic and nonorographic are defined in Figure 9.

course a simplification. In reality nonorographic waves can be generated anywhere. For example, Argentina has the most intense thunderstorms on Earth (Zipser *et al.* 2006), and their wave contribution is misclassified here. Many of the nonorographic bins also contain small islands. However, even with these caveats we chose to use the classification of orographic and nonorographic in Figure 9 because it allows us to compare the NR to previous work (Hertzog *et al.* 2008; Jewtoukoff *et al.* 2015; Vincent *et al.* 2007).

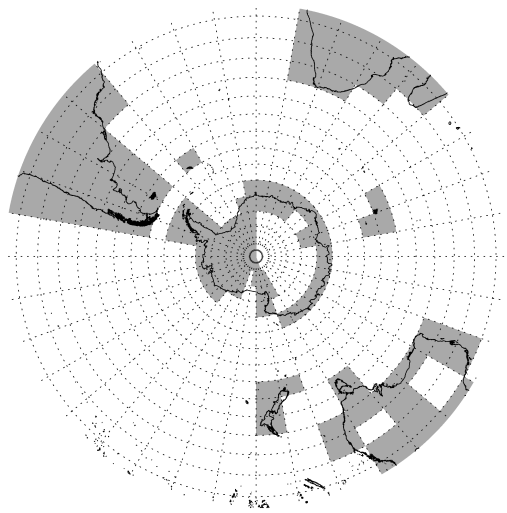

Figure 9. Orographic (gray) and nonorographic (white) bins based on the GLOBE dataset.

4. Nonorographic Gravity Wave Sources in the Southern Hemisphere in the NR

The results of Section 3 suggest that the global variations in gravity waves are quite realistic compared to observations and that nonorographic precipitation is also realistic compared to observations. To understand how nonorographic sources of gravity waves (convection and fronts in the troposphere) are contributing to the absolute gravity wave momentum flux in the lower stratosphere, in this section we investigate the relationship between precipitation and frontogenesis in the troposphere and absolute gravity wave momentum flux in the lower stratosphere in the NR for the Southern Hemisphere winter. The Southern Hemisphere winter stratosphere is the locus of larger than average climate model biases in wind and temperature (Butchart *et al.* 2011; McLandress *et al.* 2012) with important implications for modeling ozone chemistry. Because of limited land areas, the Southern Hemisphere is also a region of particular interest in

understanding nonorographic gravity wave sources (Hertzog *et al.* 2008; de la Cámara *et al.* 2014; Plougonven *et al.* 2017).

Although the validation in Section 3 showed the total fluxes in the NR are likely weaker than in nature, the realism of a model like the NR with resolved sources and waves permits an examination of the relative contributions of different sources. Figure 10 shows absolute gravity wave momentum flux in the lower stratosphere (∼15 km) for two Southern Hemisphere winter days in 2005 with proxies for nonorographic wave generation in the troposphere by convection and fronts. We chose precipitation rate and the frontogenesis function as our indicators of tropospheric wave generation. Precipitation rates are related to the strength and depth of moist convection, which is an important generation mechanism of gravity waves in the troposphere (e.g., Alexander *et al.* 1995). Fronts are also known to be a major source of gravity waves (Eckermann and Vincent 1993; Plougonven and Snyder 2007).

The absolute gravity wave momentum flux near 15 km was computed as before with Equation 3 and binned to 10° longitude × 5° latitude. We chose 15 km for the gravity wave momentum flux because it is above the level of gravity wave sources yet low enough that a significant portion of the waves will still be present. For the precipitation rate, we averaged the 0.0625° surface precipitation in each 10° longitude × 5° latitude bin. The precipitation threshold shown in Figure 10 with the thick blue contour is 0.4 mm hr^{-1}. The threshold is only shown for nonorographic regions (as defined in Figure 9). The frontogenesis function at ∼800 hPa was computed via Equation 2.1 in Charron and Manzini (2002):

$$\frac{1}{2}\frac{D|\nabla\theta|^2}{Dt} = -\left(\frac{1}{a\cos\phi}\frac{\partial\theta}{\partial\lambda}\right)^2\left[\frac{1}{a\cos\phi}\frac{\partial u}{\partial\lambda} - \frac{v\tan\phi}{a}\right] - \left(\frac{1}{a}\frac{\partial\theta}{\partial\phi}\right)^2\left[\frac{1}{a}\frac{\partial v}{\partial\phi}\right] - \left(\frac{1}{a\cos\theta}\frac{\partial\theta}{\partial\lambda}\right) \times \left[\frac{1}{a\cos\phi}\frac{\partial v}{\partial\lambda} + \frac{1}{a}\frac{\partial u}{\partial\phi} + \frac{u\tan\phi}{a}\right] \quad (5)$$

where θ is potential temperature, u is the zonal wind, v is the meridional wind, λ is longitude, and ϕ is latitude, and θ, u, and v are the large-scale fields (>1000 km here). The large-scale θ, u, and v were approximated by a spherical harmonic series truncated at horizontal wavenumber n=40 with an exponential taper. Since only coarse resolution fields were needed for the calculation, we used the 0.5° variables for this calculation. After the frontogenesis function was computed, it was binned to 10° longitude × 5° latitude. Several of the gravity wave parameterizations that tie gravity waves to sources via frontogenesis use a threshold value (e.g. Charron and Manzini 2002; Richter *et al.* 2010), although some do not (de la Cámara and Lott 2015). For the ones that do rely on a threshold, gravity waves are launched when the frontogenesis function exceeds the threshold. The value is typically somewhere between 0.045 and 0.1 K^2 (100 km)$^{-2}$ hr^{-1} (Griffiths and Reeder 1996; Charron and Manzini 2002; Richter *et al.* 2010). We chose a conservative value of 0.05 K^2 (100 km)$^{-2}$ hr^{-1}, which is shown in Figure 10 with the thick red contours for nonorographic regions.

In general the gravity wave momentum flux maxima (where the value for a bin is larger than all surrounding bins) are located inside the blue and red contours (areas with high precipitation and frontogenesis). Sometimes the precipitation and frontogenesis maxima coincide, but this is not always the case. The precipitation maxima are located predominantly between 20° and 40°S, and the frontogenesis maxima are mostly located at the higher latitudes. To evaluate the relationship between absolute gravity wave momentum flux in the lower stratosphere and precipitation and frontogenesis in the troposphere, we computed Spearman's rank correlation coefficient between precipitation and absolute gravity wave momentum flux and between the frontogenesis function and absolute gravity wave momentum flux for each geographical bin for JJA 2005. Spearman's rank correlation coefficient essentially measures the degree of monotonic relationship between two variables. We chose this method of correlation over Pearson's correlation coefficient because it does not require a linear relationship between the two variables. Visual inspection of the data revealed that a clear relationship between precipitation and gravity wave momentum flux emerges beyond precipitation values of ∼0.1 mm hr^{-1}. However, the relationship between the frontogenesis function and absolute gravity wave momentum flux is not nearly as robust as the relationship between precipitation

rate and absolute gravity wave momentum flux. While there is an obvious linear relationship between the log of the precipitation rate squared and the log of the absolute gravity wave momentum flux, there is only a weak relationship between absolute gravity wave momentum flux and the frontogenesis function and only beyond values of $\sim$0.05 K^2 (100 km)$^{-2}$ hr^{-1}. Unfortunately, this excluded a large proportion of the data from the calculation of the correlation between the frontogenesis function and absolute gravity wave momentum flux.

Figure 11 shows Spearman's rank correlation coefficient (for each nonorographic geographical bin) between absolute gravity wave momentum flux and precipitation for precipitation rates higher than 0.1 mm hr^{-1}. The higher correlations are located between 20° and 50°S, with the highest values located between 20° and 40°S in the South Pacific. This region is also the region with the most incidences of precipitation rates exceeding 10 mm hr^{-1}. These larger and more intermittent precipitation rates are associated with more intense latent heating that generates larger amplitude gravity waves.

Figure 12 shows Spearman's rank correlation coefficient (for each nonorographic geographical bin) between absolute gravity wave momentum flux and the frontogenesis function for frontogenesis function values higher than 0.05 K^2 (100 km)$^{-2}$ hr^{-1}. There are a large number of gray geographical bins in Figure 12 because there are not many bins with more than 10 data points with a frontogenesis function value higher than 0.05 K^2 (100 km)$^{-2}$ hr^{-1}. Again, this threshold was chosen based on a visual inspection of the data. The correlation coefficients in Figure 12 are much lower than the values in Figure 11, except for a few bins in the South Pacific where there is a band of higher correlations between 20° and 40°S and between 95°W and 135°W. In general, the relationship between absolute gravity wave momentum flux and the frontogenesis function is less straightforward than the relationship between absolute gravity wave momentum flux and precipitation, which is reflected in Figure 12.

Figure 13 shows the NR JJA 2005 average absolute gravity wave momentum flux in the lower stratosphere ($\sim$15 km) with the JJA averages of the proxies for nonorographic wave generation in the troposphere by convection and fronts also shown with the thick solid blue (precipitation) and red (frontogenesis) lines. Frontogenesis and precipitation are shown for nonorographic regions only. The color bar range was chosen to highlight the nonorographic gravity wave momentum flux, which is why the plot is saturated over orographic regions. Note that since these are JJA averages, the values highlighted by the red and blue solid lines are lower than the threshold values in Figure 10. Also shown in Figure 13 is where the highest precipitation rates are most common. This is highlighted with the dashed blue line, which indicates where the precipitation rate exceeds 10 mm hr^{-1} most frequently. Precipitation rates above 10 mm hr^{-1} are rare, but they are associated with strong latent heating that generates large amplitude gravity waves.

In general Figure 13 reflects the patterns shown in Figure 11 and Figure 12. Precipitation especially and fronts to some extent are relevant for gravity wave momentum flux in the South Pacific between 20° and 40°S. This coincides with the region where the nonorographic absolute gravity wave momentum flux is the highest. This area also contains a larger proportion of higher precipitation rates. In other words, the highest correlations in Figure 11 are located where the precipitation rate most frequently exceeds 10 mm hr^{-1}. Both fronts and precipitation are also correlated with gravity wave momentum flux at higher latitudes between 30 and 80°S and at most longitudes, but the correlations and absolute gravity wave momentum flux are both lower than for the South Pacific region. Additionally, Figure 13 shows that on average fronts and precipitation are fairly well correlated, especially for the areas where the precipitation rates are not likely to exceed 10 mm hr^{-1}.

The overall shape of the average precipitation rate and frontogenesis function are similar to other average measures of tropospheric wave generation. For example, Hendricks *et al.* (2014) Figure 3 shows the maximum Eady growth rate at 525 hPa averaged over 20 years of ERA-Interim data. It shows two prominent zonally elongated strips: one centered around 30°S that extends from approximately 90°W westward to 90°E and one starting at around 50°S near the eastern coast of South America that spirals poleward and eastward, almost reaching the Antarctic Peninsula in August. The main difference compared to the proxies used here is that the lower latitude maxima in the proxies in Figure 13 have a much smaller zonal extent, i.e., the proxies in Figure 13

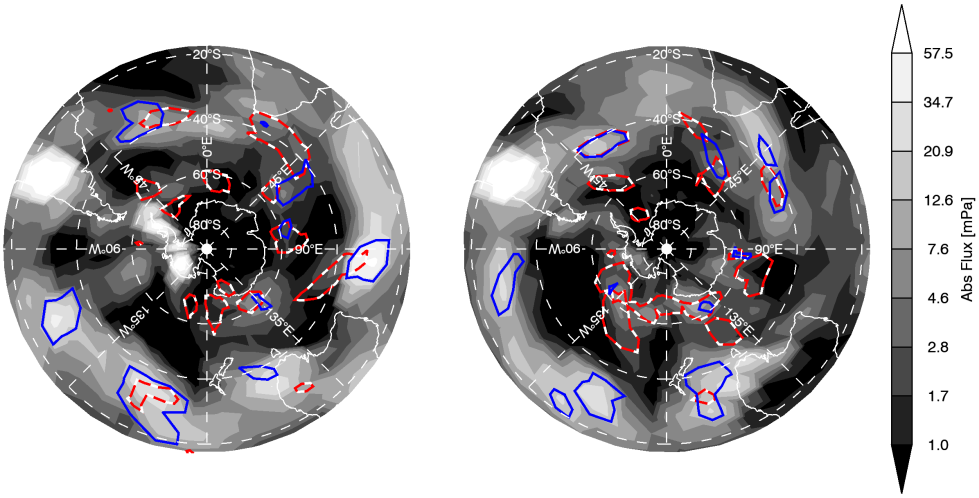

Figure 10. Gray shaded contours show absolute gravity wave momentum fluxes for two days from JJA 2005 at ∼15 km: (a) 1 June 2005 and (b) 26 July 2005. The thick solid blue line is the 0.4 mm hr^{-1} precipitation rate contour, and the thick solid red line is the 0.05 K^2 (100 km)$^{-2}$ hr^{-1} frontogenesis function contour.

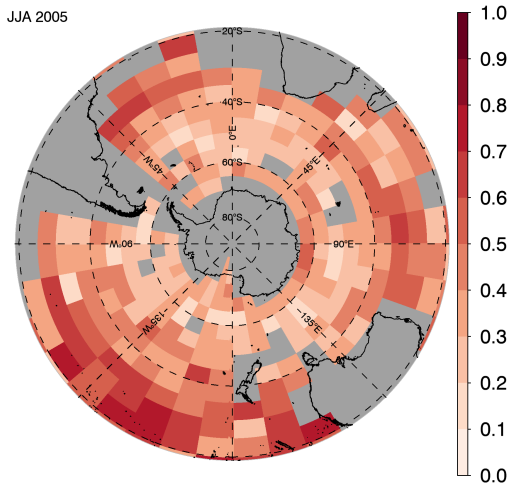

Figure 11. Spearman's rank correlation coefficient between precipitation and absolute gravity wave momentum flux for values of precipitation higher than 0.1 mm hr^{-1}. Gray areas are either bins flagged as orographic, bins for which the correlation was not significant, or bins for which there were less than 10 data points.

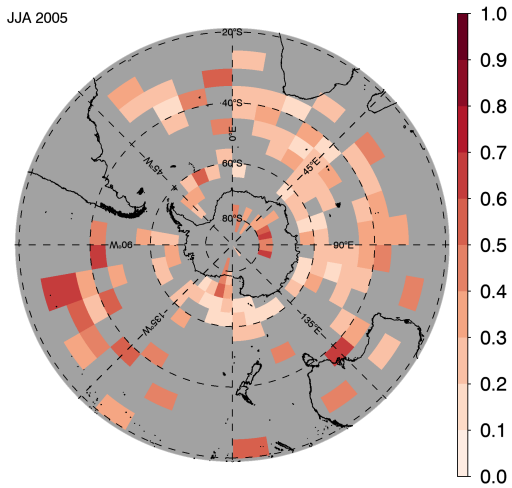

Figure 12. Spearman's rank correlation coefficient between the frontogenesis function and absolute gravity wave momentum flux for values of the frontogenesis function higher than 0.05 K^2 (100 km)$^{-2}$ hr^{-1}. Gray areas are either bins flagged as orographic, bins for which the correlation was not significant, or bins for which there were less than 10 data points.

around 30°S are not above the chosen threshold levels between 90° and 180°E.

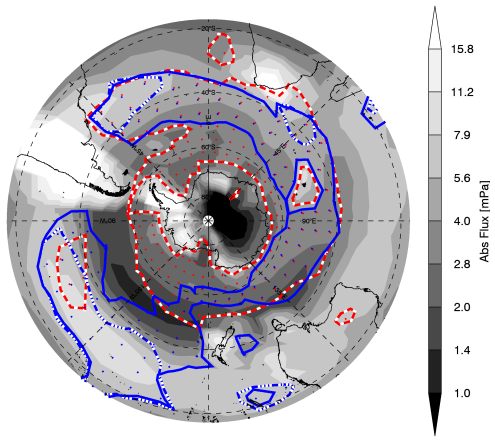

Figure 13. NR JJA average absolute momentum flux at ∼15 km. The thick solid blue line is the 0.13 mm hr^{-1} precipitation rate contour, and the thick solid red line is the 0.015 K^2 (100 km)$^{-2}$ hr^{-1} frontogenesis function contour. The dashed blue contour indicates where the precipitation rate exceeds 10 mm hr^{-1} 0.2% of the time. Stippling is on the inside of the contours.

Figure 14 shows the nonorographic zonal mean variables in Figure 13 as a function of latitude. The nonorographic gravity wave momentum flux has a maximum peak near 30°S. This peak is highly associated with the peak in intermittent precipitation (the dashed line in panel (b)). The gravity waves associated with this peak have large amplitudes and break in the lower stratosphere. Supporting this is that at ∼20 km the gravity wave momentum flux peak near 30°S is greatly diminished (shown in gray), indicating that these gravity waves have already deposited their momentum. A smaller peak in gravity wave momentum flux is located around 60°S and is more clearly associated with the peak in frontogenesis and average precipitation rate. The gravity waves associated with the 60°S peak are smaller in amplitude compared to those associated with the peak at 30°S, inferred by

the fact that the 60°S peak is only diminished by about a factor of 2 at ∼20 km.

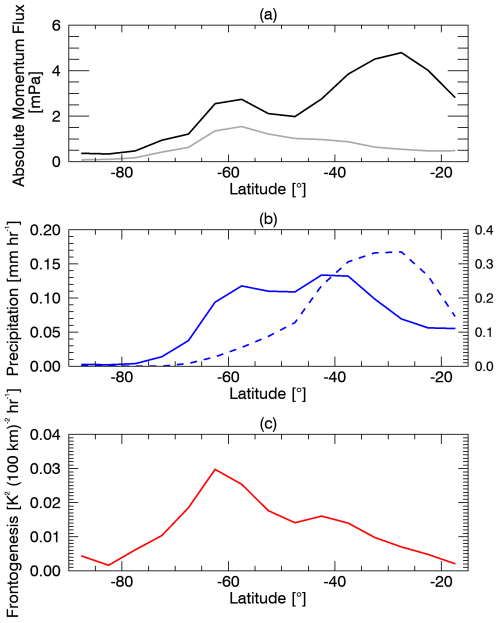

Figure 14. NR JJA average, zonal mean (a) nonorographic absolute gravity wave momentum flux at ∼15 km (black) and ∼20 km (gray), (b) precipitation rate, and (c) the frontogenesis function. The dashed blue contour in (b) indicates the percentage of time that the precipitation rate exceeds 10 mm hr^{-1}, and corresponds to the axis on the right.

5. Nonorographic vs orographic gravity waves

In Figure 13, the largest momentum fluxes are located over the Andes and the Antarctic Peninsula. However there are also large regions of elevated flux over the Southern Pacific between 20° and 40°S and near 40°S between 45°W and 90°E. These absolute values of momentum flux are not nearly as high as the orographic fluxes, but they extend over much larger geographical areas. In this section we examine the contribution to the zonal mean absolute gravity wave momentum flux over both orographic and nonorographic regions (defined in Figure 9).

Figure 15 shows the NR zonal mean of the absolute momentum flux as a function of latitude for all gravity waves, as well as the orographic and nonorographic gravity wave contribution to the total. The zonal mean absolute gravity wave momentum flux has two peaks: a high-latitude peak between 70 and 75°S and a lower-latitude peak between 25 and 30°S. The high-latitude peak is dominated by orographic gravity waves, while the lower-latitude peak is split between orographic and nonorographic gravity waves. Although absolute momentum fluxes from orographic gravity waves greatly exceed those of nonorographic gravity waves locally, the total area of the orographic gravity wave generation is much smaller than that of nonorographic waves so that the nonorographic gravity waves contribute a third of the total absolute gravity wave momentum flux.

The shapes of the lines agree well with Concordiasi observations at latitudes poleward of 50°S at 70 hPa (∼20 km) (see Figure 11a in Jewtoukoff *et al.* (2015)), but the magnitude of the NR peak near 20 km is a factor of 3 too small for the orographic contribution and between a factor of 6 and 10 too small for the nonorographic contribution (again, related to excessive dissipation). ECMWF is also shown in Figure 11 in Jewtoukoff *et al.* (2015) and also has a very similar shape, but the orographic contribution is about a factor of 7 smaller and the nonorographic contribution about a factor of 5 smaller than Concordiasi. As mentioned in Section 3.2, Jewtoukoff *et al.* (2015) removed scales larger than ∼2667 km, whereas we removed scales larger than ∼1000 km. This should be taken into consideration when comparing the values of momentum flux. If waves between 1000 and 2667 km were included in the NR gravity wave momentum flux, the values would be closer to the Concordiasi values than they currently are. We estimated this difference by including scales up to ∼2667 km (horizontal wavenumber 15) for one NR sample from JJA (August 1, 0Z), and the peak in momentum flux near 60°S increased from ∼1.7 mPa to ∼8.1 mPa. This is about a factor of 4.7 increase and suggests that the NR would be closer to a factor of 2 less than Concordiasi instead of 6–10. The shapes of the lines and magnitudes in Figure 15 also agree well with the July zonal mean gravity wave ($\lesssim$1900 km) momentum flux in Kanto (see Figure 8d in Alexander *et al.* 2016), for both orographic and nonorographic waves.

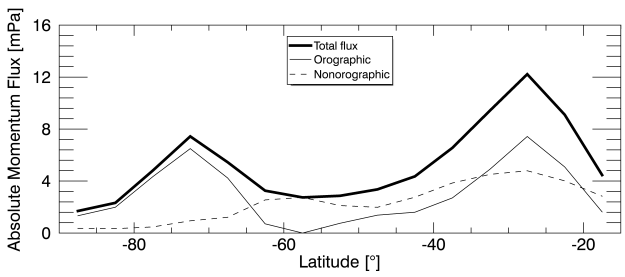

Figure 15. NR zonal mean absolute momentum flux near 15 km as a function of latitude for all waves <1000 km (thick solid line), orographic waves (thin solid line), and nonorographic waves (dashed line).

Figure 16 shows the PDFs of the JJA absolute momentum flux for orographic and nonorographic waves, where orographic and nonorographic areas are defined in Figure 9. The thin solid lines show the theoretical lognormal distribution with the mean and standard deviation of the absolute gravity wave momentum fluxes. The shapes of both orographic and nonorographic PDFs agree well with those shown previously for both balloons and models (e.g., Hertzog *et al.* 2012; Jewtoukoff *et al.* 2015; Wright *et al.* 2013). The PDFs are very similar to those from high-resolution ($0.125° \times 0.125°$) ECMWF operational analyses (see Figure 2b of Jewtoukoff *et al.* (2015)).

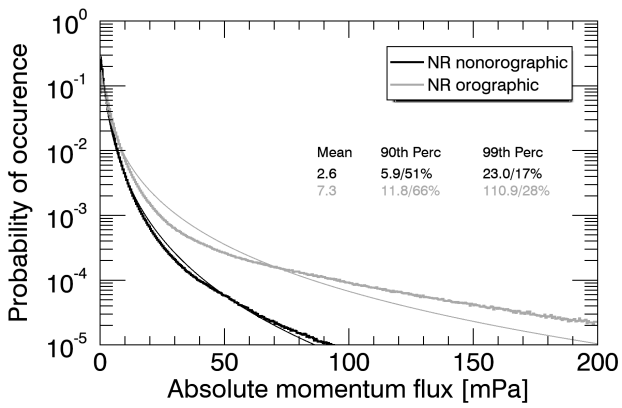

Figure 16. NR JJA PDFs of absolute momentum flux for regions over ocean (black) and over land (gray). The thin solid lines show the theoretical lognormal distributions with the same mean and standard deviation as the modeled PDFs. Also shown on the plot are the mean and the 90th and 99th percentile values for each region.

Both orographic and nonorographic gravity wave momentum flux PDFs have long tails, and the orographic PDF has a particularly long tail. The lower absolute momentum fluxes are due to smaller amplitude gravity waves that occur frequently, and the higher absolute gravity wave momentum fluxes are due to larger amplitude gravity waves that occur intermittently. The long tails of the distributions are reflected in the proportion of the total absolute momentum flux that is above 90th and 99th percentiles. For nonorographic gravity waves, 51% and 17% of the total absolute gravity wave momentum flux is attributed to fluxes above the 90th and 99th percentiles, respectively. For orographic gravity waves an even larger proportion is concentrated in the tail of the distribution, and values above the 90th and 99th percentiles account for 66% and 28% of the total absolute gravity wave momentum flux, respectively. Table 2 compares previous estimates of intermittency from various model and observational studies at various altitudes to those for the NR. All of the estimates have long tails, and the NR falls within the range of previous estimates for the 90th percentile for both orographic and nonorographic regions. For the 99th percentile, the NR has a slightly longer tail than previous estimates for both orographic and nonorographic regions. This could be because the NR estimates are at a slightly lower altitude than the other estimates.

6. Summary and conclusions

In this paper we evaluated gravity waves in the Southern Hemisphere winter in the high-resolution GEOS-5 NR by comparing brightness temperature anomalies in the NR to those in AIRS. Qualitatively the brightness temperature anomalies in the NR and AIRS have very similar global patterns, although the NR amplitudes are smaller than AIRS amplitudes. With the brightness temperature anomalies we then computed amplitudes, wavelengths, and propagation direction for both the NR and AIRS. Like other global models, the NR gravity wave amplitudes are smaller and horizontal wavelengths are longer than observed, which we attributed to excessive model dissipation. The propagation direction in the NR looks quite good compared to AIRS: both the NR and AIRS show propagation into the Southern Hemisphere winter jet.

Next we computed the absolute gravity wave momentum flux for the NR, and compared the absolute gravity wave momentum flux at 20 km to CAM5 for January and July. The NR and CAM5 have very similar global patterns of absolute gravity wave momentum flux, and the NR has a global mean value that is roughly double the CAM5 global mean. As a third evaluation of the NR, we compared precipitation rate occurrence frequencies to those from GPM. The NR nonorographic precipitation PDF compares very well with that from GPM, while the NR orographic precipitation rate occurrence frequency is considerably lower than GPM especially at the highest precipitation rates. Taken together, these comparisons suggest that while the gravity waves in the NR have weaker amplitudes and longer horizontal scales than observed, the geographic variations in gravity waves are quite realistic, and the non-orographic gravity wave sources are also realistically represented.

We further tied the absolute gravity wave momentum flux in the lower stratosphere to proxies of tropospheric nonorographic

Table 2. Estimates of intermittency from previous studies compared to the NR. Percentage of data above the 90th and 99th percentiles, a measure of how long the tails of the distributions are.

	90th percentile		99th percentile	
	Orographic	Nonorographic	Orographic	Nonorographic
NR (15 km)	66%	51%	28%	17%
Concordiasi (70 hPa; Jewtoukoff *et al.* 2015)	64%	29%		
ECMWF (70 hPa; Jewtoukoff *et al.* 2015)	72%	43%		
Vorcore (17–19 km; Hertzog *et al.* 2012)	55%	35%	26%	8%
WRF (17 km; Hertzog *et al.* 2012)	58%	46%	21%	13%
HIRDLS (25 km; Wright *et al.* 2013)	63%	56%	22%	15%

gravity wave generation: precipitation and frontogenesis. We found that intermittent precipitation is associated with absolute gravity wave momentum flux especiallly in the South Pacific between 20° and 40°S. This area has the largest percentage of high precipitation rates (exceeding 10 mm hr^{-1}). The gravity waves associated with this momentum flux peak have larger amplitudes and break below 20 km. Frontogenesis and less intermittent precipitation rates are associated with gravity wave momentum flux especially at higher latitudes near ∼60°S and with smaller amplitude waves that deposit their momentum mostly above 20 km.

Finally, we compared the orographic and nonorographic contributions to the absolute gravity wave momentum flux in the NR. We found that orographic gravity waves dominate a peak in zonal mean gravity wave momentum flux at high latitudes, and nonorographic waves contribute a third to the lower-latitude peak in zonal mean momentum flux. The PDFs of absolute momentum flux and precipitation both have long tails characteristic of the highly intermittent nature of large amplitude gravity waves. These large amplitude gravity waves break in the lower stratosphere, and are very important for the momentum budget there.

7. Acknowledgements

This work is funded by the NASA Global Modeling and Assimilation Office, Grant #NNX14O76G and the National Science Foundation, Award #1519271. This work was also supported by NASA's Modeling, Analysis and Prediction (MAP) program.

References

Alexander MJ, Barnet C. 2007. Using satellite observations to constrain parameterizations of gravity wave effects for global models. *J. Atmos. Sci.* **64**: 1652–1665, doi:10.1175/JAS3897.1.

Alexander MJ, Geller M, McLandress C, Polavarapu S, Preusse P, Sassi F, Sato K, Eckermann SD, Ern M, Hertzog A, Kawatani Y, Pulido M, Shaw TA, Sigmond M, Vincent R, Watanabe S. 2010. Recent developments in gravity-wave effects in climate models and the global distribution of gravity-wave momentum flux from observations and models. *Quart. J. Roy. Meteor. Soc.* **136**: 1103–1124, doi:10.1002/qj.637.

Alexander MJ, Holton JR, Durran DR. 1995. The gravity wave response above deep convection in a squall line simulation. *J. Atmos. Sci.* **52**(12): 2212–2226.

Alexander MJ, Teitelbaum H. 2007. Observation and analysis of a large amplitude mountain wave event over the Antarctic Peninsula. *J. Geophys. Res.* **112**: D21103, doi:10.1029/2006JD008368.

Alexander SP, Sato K, Watanabe S, Kawatani Y, Murphy DJ. 2016. Southern Hemisphere extratropical gravity wave sources and intermittency revealed by a middle-atmosphere general circulation model. *J. Atmos. Sci.* **73**: 1335–1349, doi:10.1175/JAS-D-15-0149.1.

Beres JH, Alexander MJ, Holton JR. 2004. A method of specifying the gravity wave spectrum above convection based on latent heating properties and background wind. *J. Atmos. Sci.* **61**: 324–337.

Beres JH, Garcia RR, Boville BA, Sassi F. 2005. Implementation of a gravity wave source spectrum parameterization dependent on the properties of convection in the Whole Atmosphere Community Climate Model. *J. Geophys. Res.* **110**: D10108, doi:10.1029/2004JD005504.

Butchart N, Charlton-Perez AJ, Cionni I, Hardiman SC, Haynes PH, Krüger K, Kushner PJ, Newman PA, Osprey SM, Perlwitz J, Sigmond M, Wang L, Akiyoshi H, Austin J, Bekki S, Baumgaertner A, Braesicke P, Brühl C, Chipperfield M, Dameris M, Dhomse S, Eyring V, Garcia R, Garny H, Jöckel P, Lararque JF, Marchand M, Michou M, Morgenstern O, Nakamura T, Pawson S, Plummer D, Pyle J, Rozanov E, Scinocca J, Shepherd TG, Shibata K, Smale D, Teyssèdre H, Tian W, Waugh D, Yamashita Y. 2011. Multimodel climate and variability of the stratosphere. *J. Geophys. Res.*

116: D05102, doi:10.1029/2010JD014995.

Charron M, Manzini E. 2002. Gravity waves from fronts: parameterization and middle atmosphere response in a general circulation model. *J. Atmos. Sci.* **59**: 923–941, doi:10.1175/1520-0469(2002)059⟨0923:GWFFPA⟩2.0.CO;2.

Choi HJ, Chun HY. 2013. Effects of convective gravity wave drag in the Southern Hemisphere winter stratosphere. *J. Atmos. Sci.* **70**: 2120–2136, doi:10.1175/JAS-D-12-0238.1.

de la Cámara A, Lott F. 2015. A parameterization of gravity waves emitted by fronts and jets. *Geophys. Res. Lett.* **42**: 2071–2078, doi:10.1002/2015GL063298.

de la Cámara A, Lott F, Hertzog A. 2014. Intermittency in a stochastic parameterization of nonorographic gravity waves. *J. Geophys. Res. Atmos.* **119**(21): 11,905–11,919, doi:10.1002/2014JD022002.

Eckermann SD, Vincent RA. 1993. VHF radar observations of gravity-wave production by cold fronts over Southern Australia. *J. Atmos. Sci.* **50**(6): 785–806.

Ern M, Hoffmann L, Preusse P. 2017. Directional gravity wave momentum fluxes in the stratosphere derived from high-resolution AIRS temperature data. *Geophys. Res. Lett.* **44**: 475–485, doi:10.1002/2016GL072007.

Ern M, Preusse P, Alexander MJ, Warner CD. 2004. Absolute values of gravity wave momentum flux derived from satellite data. *J. Geophys. Res.* **109**: D20103, doi:10.1029/2004JD004752.

Garcia RR, Boville BA. 1994. Downward control of the mean meridional circulation and temperature distribution of the polar winter stratosphere. *J. Atmos. Sci.* **51**: 2238–2245.

Gelaro R, Putman WM, Pawson S, Draper C, Molod A, Norris PM, Ott L, Privé N, Reale O, Achuthavavier D, Bosilovich M, Buchard V, Chao W, Coy L, Cullather R, da Silva A, Darmenov A, Errico RM, Fuentes M, kim MJ, Koster R, McCarty W, Nattala J, Partyka G, Schubert S, Vernieres G, Vikhliaev Y, Wargan K. 2015. Evaluation of the 7-km geos-5 nature run. Technical Report Series on Global Modeling and Data Assimilation, *NASA/TM-2014-104606*, Vol. 36.

Geller MA, Alexander MJ, Love PT, Bacmeister J, Ern M, Hertzog A, Manzini E, Preusse P, Sato K, Scaife AA, Zhou T. 2013. A comparison between gravity wave momentum fluxes in observations and climate models. *J. Climate* **26**: 6383–6405, doi:10.1175/JCLI-D-12-00545.1.

Gong J, Wu DL, Eckermann SD. 2012. Gravity wave variances and propagation derived from AIRS radiances. *Atmos. Chem. Phys.* **12**: 1701?1720.

Griffiths M, Reeder MJ. 1996. Stratospheric inertia-gravity waves generated in a numerical model of frontogenesis. I: Model solutions. *Quart. J. Roy. Meteor. Soc.* **122**: 1153–1174.

Hastings DA, Dunbar PK. 1999. Global land one-kilometer base elevation (globe) digital elevation model, documentation, volume 1.0. Key to Geophysical Records Documentation (KGRD) 34. National Oceanic and Atmospheric Administration, National Geophysical Data Center, 325 Broadway, Boulder, Colorado 80303, U.S.A.

Hendricks EA, Doyle JD, Eckermann SD, Jiang Q, Reinecke PA. 2014. What is the source of the stratospheric gravity wave belt in Austral winter? *J. Atmos. Sci.* **71**: 1583–1592, doi:10.1175/JAS-D-13-0332.1.

Hertzog A, Alexander MJ, Plougonven R. 2012. On the intermittency of gravity wave momentum flux in the stratosphere. *J. Atmos. Sci.* **69**: 3433–3448, doi:10.1175/JAS-D-12-09.1.

Hertzog A, Boccara G, Vincent RA, Vial F, Cocquerez P. 2008. Estimation of gravity wave momentum flux and phase speeds from quasi-Lagrangian stratospheric balloon flights. Part II: Results from the Vorcore campaign in Antarctica. *J. Atmos. Sci.* **65**: 3056–3070, doi:10.1175/2008JAS2710.1.

Hoffmann L, Alexander MJ. 2010. Occurrence frequency of convective gravity waves during the North American thunderstorm season. *J. Geophys. Res.* **115**: D20111, doi:10.1029/2010JD014401.

Hoffmann L, Alexander MJ, Clerbaux C, Grimsdell AW, Meyer CI, Rößler T, Tournier B. 2014. Intercomparison of stratospheric gravity wave observations with AIRS and IASI. *Atmos. Meas. Tech.* **7**: 4517?4537.

Hoffmann L, Spang R, Orr A, Alexander MJ, Holt LA, Stein O. 2016. A ten-year satellite record of gravity wave activity in the lower stratosphere to study polar stratospheric cloud formation. *Atmos. Chem. Phys. Discuss.* **2016**, doi:10.5194/acp-2016-757.

Hoffmann L, Xue X, Alexander MJ. 2013. A global view of stratospheric gravity wave hotspots located with Atmospheric Infrared Sounder observations. *J. Geophys. Res.* **118**: 416–434, doi:10.1029/2012JD018658.

Holt LA, Alexander MJ, Coy L, Molod A, Putman WM, Pawson S. 2016. Tropical waves and the quasi-biennial oscillation in a 7-km global climate simulation. *J. Atmos. Sci.* **73**: 3771–3783, doi:10.1175/JAS-D-15-0350.1.

Hou AY, Kakar RK, Neeck S, Azarbarzin AA, Kummerow CD, Kojima M, Oki R, Nakamura K, Iguchi T. 2014. The global precipitation measurement mission. *Bull. Amer. Meteor. Soc.* **95**(5): 701–722, doi:10.1175/BAMS-D-13-00164.1.

Jewtoukoff V, Hertzog A, Pougonven R. 2015. Comparison of gravity waves in the Southern Hemisphere derived from balloon observations and the ECMWF analyses. *J. Atmos. Sci.* **72**: 3449–3468, doi:10.1175/JAS-D-14-0324.1.

Kim SY, Chun HY, Baik JJ. 2007. Sensitivity of typhoon-induced gravity waves to cumulus parameterizations. *Geophys. Res. Lett.* **34**: L15814, doi:10.1029/2007GL030592.

Lin SJ. 2004. A 'vertically Lagrangian' finite-volume dynamical core for global models. *Mon. Wea. Rev.* **132**: 2293–2307.

McFarlane NA. 1987. The effect of orographically excited gravity wave drag on the general circulation of the lower stratosphere and troposphere. *J. Atmos. Sci.* **44**(14): 1775–1800.

McLandress C, Shepherd TG, Polavarapu S, Beagley SR. 2012. Is Missing Orographic Gravity Wave Drag near 60°S the Cause of the Stratospheric Zonal Wind Biases in Chemistry–Climate Models? *Journal of the Atmospheric Sciences* **69**(3): 802–818, doi:10.1175/JAS-D-11-0159.1.

Molod A, Takacs L, Suarez M, Bacmeister J. 2015. Development of the GEOS-5 atmospheric general circulation model: evolution from MERRA to MERRA2. *Geosci. Model Dev.* **8**: 1339–1356, doi:10.5194/gmd-8-1339-2015.

Moorthi S, Suarez MJ. 1992. A parameterization of moist convection for general circulation models. *Mon. Wea. Rev.* **120**: 3877–3886, doi:10.1029/1998JD200092.

Plougonven R, de la Cámara A, Jewtoukoff V, Hertzog A, Lott F. 2017. On the relation between gravity waves and wind speed in the lower stratosphere over the Southern Ocean. *J. Atmos. Sci.* : 1075–1093doi:10.1175/JAS-D-16-0096.1.

Plougonven R, Hertzog A, Alexander MJ. 2015. Case studies of nonorographic gravity waves over the Southern Ocean emphasize the role of moisture. *J. Geophys. Res.* **120**: 1278–1299, doi:10.1002/2014JD022332.

Plougonven R, Hertzog A, Guez L. 2013. Gravity waves over Antarctica and the Southern Ocean: consistent momentum fluxes in mesoscale simulations and stratospheric balloon observations. *Quart. J. Roy. Meteor. Soc.* **139**: 101–118, doi:10.1002/qj.1965.

Plougonven R, Snyder C. 2007. Inertia-gravity waves spontaneously generated by jets and fronts. Part I: Different baroclinic life cycles. *J. Atmos. Sci.* **64**: 2502–2520.

Plougonven R, Zhang F. 2014. Internal gravity waves from atmospheric jets and fronts. *Rev. Geophys.* **52**: 33–76, doi:10.1002/2012RG000419.

Preusse P, Ern M, Bechtold P, Eckermann SD, Kalisch S, Trinh QT, , Riese M. 2014. Characteristics of gravity waves resolved by ECMWF. *Atmos. Chem. Phys.* **14**: 10 483–10 508, doi:10.5194/acp-14-10483-2014.

Putman WM, da Silva AM, Ott L, Darmenov A. 2014. Model configuration for the 7-km GEOS-5.12 Nature Run, Ganymed Release (Non-hydrostatic 7 km Global Mesoscale Simulation). *GMAO Office Note No. 5.0 (Version 1.0)*, 18 pp., available from http://gmao.gsfc.nasa.gov/pubs/office_notes.

Putman WM, Lin SJ. 2007. Finite-volume transport on various cubed-sphere grids. *J. Computat. Phys.* **227**: 55–78.

Richter JH, Sassi F, Garcia RR. 2010. Toward a physically based gravity wave source parameterization in a general circulation model. *J. Atmos. Sci.* **67**: 136–156, doi:10.1175/2009JAS3112.1.

Sardeshmukh PD, Hoskins BJ. 1984. Spatial smoothing on the sphere. *Mon. Wea. Rev.* **112**: 2524–2529.

Sato K, Watanabe S, Kawatani Y, Tomikawa Y, Miyazaki K, Takahashi M. 2009. On the origins of mesospheric gravity waves. *Geophys. Res. Lett.* **36**: L19801, doi:10.1029/2009GL039908.

Seto S, Iguchi T, Oki T. 2013. The basic performance of a precipitation retrieval algorithm for the global precipitation measurement mission's single/dual-frequency radar measurements. *IEEE Trans. Geosci. Remote Sens.* **51**(12): 5239–5251, doi:10.1109/TGRS.2012.2231686.

Song IS, Chun HY. 2005. Momentum flux spectrum of convectively forced internal gravity waves and its application to gravity wave drag parameterization. Part I: Theory. *J. Atmos. Sci.* **62**: 107–124, doi:10.1175/JAS-3363.1.

Tokioka T, Yamazaki K, Kitoh A, Ose T. 1988. The equatorial 30?60 day oscillation and the Arakawa-Schubert penetrative cumulus parameterization. *J. Meteor. Soc. Japan* **66**: 883–901.

Vincent RA, Hertzog A, Boccara G, Vial F. 2007. Quasi-Lagrangian superpressure balloon measurements of gravity-wave momentum fluxes in the polar stratosphere of both hemispheres. *Geophys. Res. Lett.* **34**: L19804, doi:10.1029/2007GL031072.

Watanabe S, Kawatani Y, Tomikawa Y, Miyazaki K, Takahashi M, Sato K. 2008. General aspects of a T213L256 middle atmosphere general circulation model. *J. Geophys. Res.* **113**: D12110, doi:10.1029/2008JD010026.

Wei J, Zhang F. 2014. Mesoscale gravity waves in moist baroclinic jet-front systems. *J. Atmos. Sci.* **71**: 929–952, doi:10.1175/JAS-D-13-0171.1.

Woods BK, Smith RB. 2010. Energy flux and wavelet diagnostics of secondary mountain waves. *J. Atmos. Sci.* **67**: 3721–3738, doi:10.1175/2009JAS3285.1.

Wright CJ, Osprey SM, Gille JC. 2013. Global observations of gravity wave intermittency and its impact on the observed momentum flux morphology. *J. Geophys. Res.* **118**: 10 980–10 993, doi:10.1002/jgrd.50869.

Zipser E, Liu C, D C, Nesbitt SW, Yorty S. 2006. Where are the most intense thunderstorms on Earth? *Bull. Amer. Meteor. Soc.* **87**: 1057–1071.